Molecular Visualization of Neuronal TDP43 Pathology *In Situ*

Authors: Amanda L. Erwin[1,2†], Martin G. Fernandez[1,3†], Durga Attili[1,2,4], Matthew L. Chang[1], Michael Bekier[4], Emile S. Pinarbasi[4,5], Jennifer E. Russ[6], Renaldo Sutanto[1,2], Dafydd Thomas[5], Xinfei Shen[7], Ryan D. Baldridge[6,8], Elizabeth M. H. Tank[4], Sami J. Barmada[4*], Shyamal Mosalaganti[1,2,3,6*]

Affiliations:

[1] Life Sciences Institute, University of Michigan, Ann Arbor, MI, 48109, United States

[2] Department of Cell and Developmental Biology, University of Michigan, Ann Arbor, MI, 48109, United States

[3] Department of Biophysics, College of Literature, Science and the Arts, University of Michigan, 48109, United States

[4] Department of Neurology, University of Michigan, Ann Arbor, MI, 48109, United States

[5] Department of Pathology, Michigan Medicine, University of Michigan, Ann Arbor, MI, 48109, United States

[6] Department of Biological Chemistry, University of Michigan, Ann Arbor, MI, 48109, United States

[7] Department of Biomedical Engineering, University of Michigan, Ann Arbor, MI, 48109, United States

[8] Cellular and Molecular Biology Program, University of Michigan Medical School, Ann Arbor, MI, 48109, United States

[†]These authors contributed equally to the work

*Corresponding authors: sbarmada@med.umich.edu, mosalaga@umich.edu

Abstract:

Nuclear exclusion and cytoplasmic accumulation of the RNA-binding protein TDP43 are characteristic of amyotrophic lateral sclerosis (ALS) and frontotemporal lobar degeneration (FTLD). Despite this, the origin and ultrastructure of cytosolic TDP43 deposits remain unknown. Accumulating evidence suggests that abnormal RNA homeostasis can drive pathological TDP43 mislocalization, thereby enhancing RNA misprocessing due to the loss of nuclear TDP43, and engendering a cycle that ultimately leads to cell death. Here, we demonstrate that the addition of small monovalent oligonucleotides successfully recapitulates pathological TDP43 mislocalization and aggregation, aberrant splicing, and degeneration in iPSC-derived neurons (iNeurons). By employing a tailored multimodal *in situ* cryo-correlative light and electron microscopy pipeline, we examine the localization and aggregation of TDP43 in near-native conditions. We discover that mislocalized TDP43 accumulates and forms ordered fibrils within autophagosomes and lysosomes in iNeurons, as well as in ALS/FTLD patient tissue. We also provide the first high-resolution snapshots of TDP43 aggregates *in situ*, delivering an unprecedented view of the earliest pathogenic events underlying ALS, FTLD, and related TDP43 proteinopathies.

Introduction

Trans-active response DNA/RNA binding protein of 43 kDa (TDP43) is a ubiquitously expressed nuclear protein responsible for RNA splicing, transport, and stability that is integrally linked with amyotrophic lateral sclerosis (ALS) and frontotemporal lobar degeneration (FTLD)[1–4]. Nearly 95% of individuals with ALS and ~50% of those with FTLD exhibit nuclear exclusion and cytosolic aggregation of TDP43 within affected neurons and glia[5]. TDP43 mislocalization and cytosolic aggregation are not limited to ALS and FTLD; TDP43 pathology is increasingly recognized as a common event in elderly patients with slowly progressive cognitive decline, termed limbic predominant age-related TDP43 encephalopathy (LATE)[6]. Once excluded from the nucleus, TDP43 primarily accumulates within cytoplasmic aggregates[7,8]. Within cortical regions, these deposits contain amyloidogenic C-terminal TDP43 fragments[9–11], while spinal cord inclusions are rich in full-length TDP43[12]. These observations suggest that the TDP43 aggregate composition, the mechanisms underlying their formation, and downstream consequences may differ depending on the brain region involved.

Despite its prevalence and increasingly recognized connection with disease pathogenesis, the origin of TDP43 mislocalization and the architecture of native TDP43 inclusions within intact tissue remain mysterious. Engineered mutations disrupting the nuclear localization signal of TDP43[13–15], application of exogenous stressors[16,17], addition of recombinant TDP43 fibrils[18,19], or the use of artificial aggregation-promoting domains can all elicit TDP43 mislocalization[20]; yet, these circumstances are disconnected from the pathophysiology of the disease. More recent discoveries suggest that RNA is one of the most significant determinants of TDP43 localization[21–23]. In light of the extensive and widespread abnormalities in RNA processing identified in ALS/FTLD patient material and models[24–26], this observation raises the intriguing possibility that RNA dysregulation may underlie TDP43 mislocalization and aggregation in these conditions.

Here, we demonstrate that prolonged application of RNA oligonucleotides leads to TDP43 mislocalization, cryptic splicing, neurotoxicity, and the formation of cytosolic TDP43 inclusions in human neurons, resembling aggregates characteristic of human disease. Moreover, cytosolic TDP43 aggregates accumulate primarily within autophagosomes and lysosomes, indicating that these organelles play a crucial role in the formation and/or clearance of mislocalized TDP43. Combining cryogenic-correlative light and electron microscopy (cryo-CLEM) and cryo-electron tomography (cryo-ET), we demonstrate that autophagosomal and lysosomal TDP43 adopts filamentous morphologies mirroring those detected in ALS and FTLD with TDP43 pathology (FTLD-TDP)[27,28]. In keeping with these observations, we detected abundant TDP43 filaments within ALS/FTLD patient tissue-derived lysosomes. Based on these observations, we propose that RNA dyshomeostasis, in conjunction with ineffective autophagy or lysosomal turnover — processes often impaired in aging[29–36] — could contribute to nuclear TDP43 mislocalization and the accumulation of fibrillar aggregates characteristic of TDP43 proteinopathies such as ALS and FTLD-TDP.

Results

Establishing an in vitro neuronal model to recapitulate TDP43 pathology

Short oligonucleotides (oligos) bearing GU motifs, which are recognized by TDP43 RNA recognition motifs (RRM1-2), effectively promote TDP43 nuclear efflux in transformed cell lines[21–23]. To study a cell type relevant to ALS and FTLD, we applied short, monovalent GU-rich RNA (5'-

GUGUGUGUGUGU-3', $(GU)_6$ hereafter) to human induced pluripotent stem cell (iPSC) derived neurons (iNeurons). All oligonucleotides were modified by 2'-*O*-methyl and phosphorothioate (PS) groups to enhance resistance to RNase degradation. A customized cassette encoding the master transcription factors NGN1 and NGN2, under the control of a doxycycline (dox)-inducible promoter, was integrated into the *CLYBL* safe harbor locus of iPSCs, facilitating robust and rapid differentiation of iPSCs into glutamatergic, forebrain-like iNeurons (**Fig. 1A**)[25,37–42]. $(GU)_6$ oligos were transfected using Endo-Porter into iNeurons before the assessment of TDP43 localization by immunostaining and fluorescence microscopy. In contrast to the rapid (<6h) effect of RNA oligonucleotides on TDP43 localization in transformed cell lines[21–23], we observed mislocalization and cytosolic accumulations of TDP43 in iNeurons only after 24h or more of $(GU)_6$ treatment (**Fig. 1B, C; Fig. S1C, D**). We did not observe such mislocalization in untreated iNeurons or those exposed to Endo-Porter alone or Endo-Porter with control RNA oligos (5'-CCCCCCCCCCCC-3', C_{12} hereafter) (**Fig. 1B-D, and Fig. S1A-D**). By 24h post-$(GU)_6$ treatment, approximately half of all iNeurons displayed a greater than 50% reduction in their nuclear-to-cytoplasmic TDP43 ratio (**Fig. 1C, D**). Based on these kinetics, we chose the 24h time point for all subsequent experiments.

Loss of nuclear TDP43 in disease results in distinct splicing changes, including the abnormal inclusion of unannotated and non-conserved (cryptic) exons in TDP43 target RNAs. We therefore assessed whether treatment with $(GU)_6$ oligos triggered cryptic splicing of TDP43 substrates that are consistently affected in ALS and FTLD-TDP[43,44]. Cryptic products of *ARHGAP32, HDGFL2, STMN2,* and *SYT7* were dramatically upregulated in iNeurons upon treatment with $(GU)_6$ for 24h (**Fig. 1E**), consistent with a decrease in the TDP43 nuclear-to-cytoplasmic ratio in these cells (**Fig. 1C, D**). We also observed significant cryptic splicing with the proteasome inhibitor MG132, consistent with the rapid mislocalization of TDP43 triggered by this compound[45,46]. These results confirm that RNA-induced TDP43 mislocalization in iNeurons is associated with the loss of nuclear TDP43 splicing activity.

A central and defining feature of neurodegenerative diseases such as ALS and FTLD is the progressive loss of neurons in affected brain regions. To determine whether $(GU)_6$-dependent TDP43 mislocalization leads to neuron loss, we employed automated longitudinal microscopy to assess the fate of individual iNeurons treated with oligonucleotides[25,47]. iNeurons treated with Endo-Porter, Endo-Porter and C_{12}, or Endo-Porter and $(GU)_6$ oligos were imaged at regular 24h intervals over 10d by automated microscopy. We applied semantic image segmentation algorithms to detect individual neurons in the images. For each neuron, the time of death was defined using a red-shifted genetically encoded death indicator (RGEDI)[48] that fluoresces only when intracellular Ca^{2+} rises rapidly. Cell death was also marked by morphological changes, such as rounding of the soma, neurite retraction, and blebbing (**Fig. 1F**). Using this assay, we found that treatment with either C_{12} and $(GU)_6$ oligos significantly increased the risk of death compared to no treatment or Endo-Porter alone, suggesting mild non-specific toxicity associated with RNA transfection in neurons (**Fig. 1G**). Consistent with the selective impact of $(GU)_6$ oligos on TDP43 localization, however, we observed the highest risk of death in neurons treated with $(GU)_6$ **(Fig. S1G)**.

We also examined oligo-treated iNeurons for post-translational modifications typical of mislocalized TDP43 in ALS and FTLD-TDP. Similar to pathological TDP43 aggregates[3,7,8,49], cytoplasmic TDP43 puncta are phosphorylated (S409/S410) and ubiquitinated (**Fig. S2**). These modifications were only observed after 10d, however, suggesting that phosphorylation and

ubiquitination are delayed effects rather than primary contributors to TDP43 aggregation. Taken together, these findings indicate that RNA-induced perturbation of TDP43 localization in iNeurons recapitulates key features of ALS/FTLD-TDP pathology, including TDP43 nuclear egress, aberrant splicing, and neuronal loss[7,43,44,50].

A custom cryo-CLEM workflow to visualize mislocalized TDP43 in situ

Given the strong genetic and mechanistic links between ALS/FTLD and dysfunction of the autophagosome–lysosome system[51–54], we hypothesized that these organelles may play a pivotal role in the sequestration and clearance of mislocalized TDP43. While light microscopy enables tracking of protein dynamics, it lacks the ultrastructural resolution required to visualize the subcellular context and organization of pathological protein assemblies. To overcome this limitation and interrogate the native architecture of mislocalized TDP43 in human iNeurons, we established a robust *in situ* cryo-correlative light and electron microscopy (cryo-CLEM) workflow. This approach integrates the molecular specificity of fluorescence imaging with the nanometer resolution of cryo-electron tomography, enabling precise spatial correlation of TDP43 within an intact cellular environment (**Fig. 2**). To specifically visualize neuronal lysosomes with cryo-CLEM, iPSCs were differentiated into iNeurons as before (**Fig. 1A**), but on micropatterned gold electron microscopy grids (**Fig. 2A**). The grids are manually screened for consistency in neuron distribution and quality (cell density, presence of neurites, etc.) using a standard widefield microscope. This is crucial for imaging and obtaining high-resolution insights from morphologically healthy neurons, as, unlike other mammalian cell types, grids containing iNeurons exhibit a high degree of heterogeneity. After treating iNeurons with Endo-Porter and $(GU)_6$ for 24h, we added LysoTracker Green DND-26, a fluorescent weak base that selectively accumulates in acidic organelles such as lysosomes. Due to the properties of the dye and the dynamic behavior of the endolysosomal system, LysoTracker also labels other acidified organelles in this pathway. As these structures are morphologically indistinguishable in cryo-electron tomograms, we will collectively refer to endolysosomes, autolysosomes, and terminal lysosomes as lysosomes throughout this study. Within 5m of the addition of LysoTracker, FluoSpheres were added for fiducial-based correlation, and the grids were plunge-frozen in liquid ethane. LysoTracker was employed to visualize lysosomes with cryo-CLEM, taking advantage of the fact that dyes are far brighter and yield less background than GFP or its spectral variants. We collected cryo-confocal z-stacks of candidate iNeurons (**Fig. 2B**) and subsequently transferred autogrids containing cells to a dual-beam cryo-focused ion beam scanning electron microscope (cryo-FIB/SEM). We then used the 3D Correlation Toolbox to precisely target the region of interest based on the cryo-confocal images (**Fig. 2B, C**)[55]. Following cryo-focused ion beam (cryo-FIB) milling, the lamella were assessed by cryo-TEM, allowing for a second correlation of the fluorescence plane, previously identified from 3DCT correlation (**Fig. 2C**), with the medium magnification cryo-TEM image (6500×, **Fig. 2D**). Tilt-series data collection, followed by tomogram reconstruction on areas guided by the fluorescence signal, revealed the presence of filaments within lysosomes of $(GU)_6$-treated iNeurons (**Fig. 2E, Movie 1)**.

In situ TDP43 architecture at molecular resolution

Lysosomes are dynamic, heterogeneous organelles whose contents may vary considerably even within the same compartment and subcellular location[56]. Evidence for this is clear in **Fig. 2**; although the field of view contains two lysosomes marked by LysoTracker fluorescence, several fibrils are visible in the lysosome at the top of the field, while the centrally located lysosome is devoid of any fibrillar material (**Fig. 2E,** *Lyso. 1 vs. Lyso. 2*). To determine if these filaments are comprised of TDP43, we employed CRISPR/Cas9 to insert an open reading frame encoding HaloTag immediately downstream of the endogenous *TARDBP* start codon in human iPSCs, thereby generating a fusion of HaloTag with the N-terminus of native TDP43 (**Fig. S4A**). The correct positioning of HaloTag was confirmed by Sanger sequencing, and an appropriate shift in the molecular weight of TDP43 was observed on immunoblotting (**Fig. S4B**). After integrating the *NGN1/NGN2* cassette, HaloTag-TDP43 iPSCs were differentiated into iNeurons as above and labeled using a cell-permeable and photostable HaloTag-compatible dye (JF635)[57]. We then applied GU_6 oligos for 24h and employed our cryo-CLEM workflow to visualize mislocalized, JF635-positive HaloTag-TDP43 puncta within the cytoplasm in greater detail (**Fig. S4C-E**). Some of these HaloTag-TDP43 foci appeared to have very little organized ultrastructure, instead forming amorphous accumulations of various sizes that excluded ribosomes and other cellular organelles (**Fig. 3A, Movie 2**). Fluorescence signals from Halo-TDP43 often overlapped with these puncta, suggesting that these structures may represent phase-separated condensates. Notably, such 'ribosome-excluded zones' frequently localize to the surface of lysosomes, where they adopt the curvature of the adjacent membrane. (**Fig. 3A, Movie 1**). We also observed several larger cytosolic TDP43 foci located within double membrane-bound structures reminiscent of autophagosomes (**Fig. 3B, Movie 2**). TDP43-containing autophagosomes also exhibit a variety of other cellular debris or amorphous material, consistent with bulk (macro) autophagy of TDP43 fibrils.

A significant portion of mislocalized TDP43 appeared to be fibrillar rather than amorphous and was present within single, membrane-bound lysosomes (**Fig. 3C, Movie 3**). Within these organelles, the density and size of TDP43 filaments varied considerably (**Fig. 3C**). Overall, we observed TDP43 fibrils within ~25% of imaged lysosomes (n = 133) and ~12% of autophagosomes (n = 46). We classified the lysosomes based on the luminal content into either 'empty', i.e., electron translucent, with no visible electron dense material within the lumen; 'non-fibrillar', containing amorphous or membranous material; or 'fibrillar', containing bona fide filaments or fibrils (**Fig. S5A, B**). Because it is challenging to identify fibrils within the amorphous 'condensate-like' deposits, the presence of smaller filaments cannot be completely ruled out within these regions. Nevertheless, we did not find TDP43 filaments outside of acidified membrane-enclosed organelles such as lysosomes and autophagosomes, suggesting that fibril formation may be enhanced by changes in pH, molecular crowding, and/or partial cleavage of TDP43 within these organelles[58].

We next assessed the size of fibril-containing lysosomes across cryo-ET data collected from Halo-TDP43 iNeurons treated with $(GU)_6$ oligos. Despite the broad distribution of lysosome size, we observed that lysosomes containing fibrils were significantly larger when compared to the empty or non-fibrillar lysosomes (**Fig. 3D**). Additionally, we observed a clear correlation between longer fibrils and predominantly larger lysosomes and autophagosomes (**Fig. S5C**). To further characterize these fibrils, we measured their width and found an average of 5.5 ± 0.61nm (**Fig.**

3E). This value closely matches the mean width of amyloidogenic C-terminal fibrils of TDP43 obtained by proteinase K-mediated digestion (5.4 ± 1.5nm), and the pronase-treated sarkosyl insoluble fibrils obtained from FTLD Type A, suggesting that intralysosomal TDP43 fibrils undergo partial proteolysis[27,59].

Mislocalized TDP43 accumulates within autophagosomes and lysosomes in other cell types

TDP43 mislocalization is not limited to neurons in ALS and FTLD-TDP but is also found in glia and other CNS cell types. We therefore investigated whether TDP43 demonstrates similar accumulation within autophagosomes and lysosomes of non-neuronal cells upon treatment with $(GU)_6$ oligos. To do so, we utilized an engineered HEK293T cell line in which the endogenous *MAP1LC3B* gene was fused to an open reading frame encoding the photoconvertible fluorescent protein Dendra2[39]. As in iNeurons, we used Endo-Porter to treat Dendra2-LC3B HEK293T with Endo-Porter alone (control) or Endo-Porter and $(GU)_6$ oligos. After 4h, we isolated Dendra2-positive autophagosome-rich and lysosomal-rich fractions by density gradient centrifugation and immunoblotted for TDP43 content within each fraction (**Fig. 4A, Fig. S6A)**. We observed a significant shift in the distribution of TDP43 upon Endo-Porter and $(GU)_6$ oligo treatment towards lysosomal and autophagosomal fractions (**Fig. 4A**). Treating HEK293T cells with Endo-Porter alone (control) failed to induce a similar effect (**Fig. 4A**), confirming that the observed shift of TDP43 towards autophagosomal and lysosomal fractions is specific for $(GU)_6$.

To confirm this, we prepared ultrathin sections of high-pressure frozen and freeze-substituted Dendra2-LC3B HEK293T cells, allowing us to examine RNA-induced TDP43 mislocalization by immuno-electron microscopy (immuno-EM). Gold-labeled anti-TDP43 antibodies reaffirmed the presence of TDP43 within single membrane-bound lysosomes (**Fig. 4B).** Membrane-bound vesicles exhibited significantly more gold beads in $(GU)_6$-treated cells in comparison to cells treated with Endo-Porter alone (control), indicative of greater lysosomal TDP43 immunoreactivity following RNA application **(Fig. S7)**.

We also isolated sarkosyl-insoluble fractions from control and $(GU)_6$-treated Dendra2-LC3B HEK293T cells to assess for TDP43 fibrils analogous to those detected in iNeurons (**Fig. S6B**). Negative stain transmission electron microscopy (TEM) of these samples revealed the presence of fibrils, reminiscent of TDP43 filaments obtained from post-mortem brain tissue[27,28], but only in the $(GU)_6$-treated samples. Immunogold labeling with TDP43-specific antibodies once again confirmed that these fibrils are comprised of TDP43 (**Fig. 4C**). To probe if fibrils are already present in isolated organelles, and to verify that they are not an artifact of sarkosyl extraction, we performed cryo-CLEM on plunge-frozen lysosomal and autophagosomal fractions isolated from Dendra2-LC3B HEK293T cells treated with $(GU)_6$ oligos (**Fig. 4D, S6C**). In these samples, Dendra2-LC3B fluorescence enabled the precise localization of autophagosomes and lysosomes. Subsequent cryo-ET tilt-series data collection from these areas, followed by tomogram reconstruction, revealed multiple filaments ensconced within membrane-bound organelles (red arrows, **Fig. 4D, S6C**). These filaments displayed a mean width of 4.9 ± 0.79nm, mirroring both iNeuron intralysosomal filaments and the amyloidogenic C-terminus of TDP43 obtained by limited proteolysis of the protein[59] **(Fig. 3E)**.

TDP43 mislocalizes to autophagosomes and lysosomes in ALS patient tissue

Our observations of TDP43 fibrils within autophagosomes and lysosomes suggest that the earliest stages of pathological TDP43 deposition may occur within these organelles. To pursue this

possibility, we performed dual immunohistochemistry for TDP43 and markers of lysosomes (LAMP1) or autophagosomes (LC3B) in ALS patient spinal cord sections. Within the patient tissue, we stratified motor neurons based on the TDP43 signal within the nucleus. Spinal motor neurons within the anterior horn, characterized by a strong nuclear TDP43 signal, 'ALS-nuclear TDP43', resemble healthy neurons and exhibit the expected distribution of LAMP1 and LC3B within the cytosol. However, spinal motor neurons with pathological nuclear exclusion of TDP43, 'ALS-cytoplasmic TDP43', displayed a marked overlap of cytoplasmic TDP43 puncta with lysosomes, and to a lesser extent, autophagosomes (**Fig. 5A**). Similar to 'ALS-nuclear TDP43' motor neurons, we did not observe any overlap of fluorescence signals between TDP43 and lysosomes or autophagosomes in spinal motor neurons from control subjects (**Fig. S8A, B**). The overlap between TDP43 and these organelles was further confirmed by immunofluorescence microscopy in neurons displaying TDP43 mislocalization, but not in neurons with nuclear TDP43 or in neurons from control patients (**Fig. 5B and Fig. S8C, D)**. Quantification of control and ALS patient tissue confirmed a significant increase in TDP43 colocalization with LAMP1 in diseased neurons (**Fig. 5C)**. On the contrary, colocalization of TDP43 with the autophagosomal marker LC3B was significantly higher in control neurons than in patient neurons (**Fig. 5D**), suggesting that TDP43 may be actively cleared or eliminated by these organelles.

To verify the accumulation of mislocalized TPD43 within autophagosomes and lysosomes of post-mortem patient material, we adapted the method we previously used for isolating these organelles from cultured cells and used it to fractionate ALS/FTLD-TDP prefrontal cortex (**Fig. 6A; Fig. S6A**). In lysosome-rich fractions, we detected full-length and phosphorylated TDP43 (S409/S410) as well as truncated species of ~35 and 25 kDa **(Fig. 6B**). Cryo-ET analysis of these lysosomes revealed filamentous inclusions within membrane-bound structures that were remarkably similar to what we observed in iNeurons and HEK293T cells (**Fig. 6C**). The widths of filaments in patient-derived lysosomes displayed a bimodal distribution, ranging from 5-15nm (**Fig. 6D, E**). These filaments most likely represent distinct, partially proteolyzed states of TDP43. Finally, we extracted sarkosyl-insoluble material from patient-derived brain lysosomes (**Fig. S6B**). We probed for phosphorylated TDP43 by immunoelectron microscopy (immuno-EM). We observed filaments decorated with gold beads, confirming the presence of TDP43-positive fibrillar deposits within the lysosomes of human patient brain tissue (**Fig. 6F**). Together, these findings validate and extend our observations from $(GU)_6$-treated iNeurons, suggesting that RNA dysregulation may similarly foster TDP43 mislocalization and aggregation in disease.

Discussion

TDP43 recognizes nearly one-third of all transcribed genes and is crucial for diverse aspects of RNA metabolism[60,61]. Loss of this protein from the nucleus and its cytosolic accumulation are closely tied to neurodegeneration in cellular and animal models of ALS/FTLD-TDP, as well as in human post-mortem samples[14,53,62]. Indeed, TDP43 knockdown leads to dramatic and widespread changes in RNA splicing and stability[24,43,44,63–65], implying that RNA misprocessing in ALS/FTLD-TDP is downstream of TDP43 mislocalization. Our data, together with recent studies highlighting the significance of RNA for TDP43 localization[21–23], are consistent with an alternative possibility: RNA dyshomeostasis may precede and drive TDP43 mislocalization, thereby eliciting a self-perpetuating positive feedback loop that further facilitates and enhances RNA misprocessing. The result is a spiral of RNA dysfunction and TDP43 mislocalization that expedites neuronal toxicity and degeneration in disease.

RNA misprocessing may originate from genetic and/or acquired means. For instance, mutations in genes encoding RNA-binding proteins, such as FUS, hnRNPA2B1, MATR3, and TDP43, themselves lead to ALS and FTLD-TDP[66–72]. Co-transcriptional RNA modifications, including methylation at the N^6 position of adenosine (m^6A), may also affect TDP43 binding affinity and/or the fate of transcribed RNA[25,73–76]. Abnormal RNA methylation is characteristic not only of ALS and FTLD-TDP but also other conditions, such as Alzheimer's disease, that display TDP43 pathology[25,26,77–79]. RNA-based sequestration of TDP43 into cytosolic granules is also observed during skeletal muscle regeneration in mice and humans[80]. These myo-granules are rich in fibrillar TDP43, suggesting common misfolding events upon cytosolic TDP43 mislocalization. Here, we used TDP43 substrate, specifically GU-rich RNA oligos, to initiate the efflux of TDP43 from the nucleus in iNeurons (**Fig. 1A-D and Fig. S1**). Treated iNeurons accumulate cryptic isoforms from TDP43-targeted transcripts and display progressive toxicity with time (**Fig. 1E**), effectively recapitulating key hallmarks of the pathophysiology of ALS/FTLD.

Biochemical fractionation experiments revealed the presence of full-length TDP43 within autophagosomes and lysosomes of short GU-rich oligo-treated cells (**Fig. 4**). This is consistent with the appearance of full-length TDP43 within pathological aggregates in ALS spinal motor neurons[12], the overlap between TDP43 inclusions and lysosomal markers in post-mortem ALS samples (**Fig. 5C, D**), the visualization of TDP43 filaments within autophagosomes and lysosomes in iNeurons (**Figs. 2E, 3B, C**), and the appearance of filaments in purified lysosomes from ALS/FTLD-TDP brain (**Fig. 6C**). Collectively, these data imply that mislocalized TDP43 accumulates and misfolds within acidified organelles. Future investigations may focus on whether the fibrils represent pathological intermediates capable of seeding further TDP43 aggregation, as well as the factors governing the formation and/or degradation of such intermediates.

Structural studies on purified protein fragments or fibrils extracted from patient samples are invaluable for deriving small-molecule ligands or tracers specific for protein inclusions; nevertheless, these investigations are limited in their ability to uncover molecular mechanisms of TDP43 aggregation. To address this, we established an *in situ* cryo-CLEM platform (**Fig. 2**), which provides the first visual snapshots of endogenous TDP43 mislocalization and aggregation within human neurons. Application of short GU-rich oligos leads to the appearance of amorphous 'condensate-like' TDP43 inclusions within the cytosol (**Fig. 3A, Movie 2**), whose material properties may depend on chaperones (i.e., HSPB1)[81] and/or RNA length, size, modifications, and motif valency[82]. Cytosolic TDP43 condensates were often found in association with lysosomal membranes, but within these organelles, TDP43 adopts filamentous structures (**Fig. 3C, Movie 2, 3**). The acidified environment of lysosomes may promote the demixing of TDP43 from condensates, leading to its misfolding and filament formation[83–85]. The appearance of TDP43 within autophagosomes argues against chaperone-mediated autophagy in the clearance of cytosolic TDP43[86] but would be consistent with bulk macroautophagy. Additionally, we cannot rule out the possibility of selective autophagy of fibrillar TDP43[87,88], involving an as-yet-unidentified adapter. Prior studies identified a single LC3-interacting region (LIR)-containing protein in association with TDP43—TATA-box binding protein (TBP)[89]—but further studies are required to determine whether this factor is necessary for the delivery of cytosolic TDP43 to lysosomes and/or autophagosomes.

The TDP43 C-terminal low complexity domain (LCD) is critical for forming pathological amyloid-like aggregates *in vitro*. Within this region, amino acid stretches 286-331 in primary cortical

neurons[90], and 341-367 in neuronal cell lines are sufficient for fibril formation[9,10]. Here, we show that introducing GU-rich oligos reproduces TDP43 mislocalization and aggregation within human neurons and cell lines. Mislocalized TDP43 forms fibril-like structures reminiscent of patient-derived fibrils, mainly in autophagosomes and lysosomes, underscoring the importance of these acidified organelles in the formation and/or clearance of nascent TDP43 aggregates (**Fig. 3**). The exact nature of TDP43 species within lysosomal/autophagosomal fibrils, and whether these structures sequester specific RNAs or proteins, remains to be investigated.

Based on these observations, we propose a model for TDP43 mislocalization, clearance, and its aggregation in disease (**Fig. 7**). External stressors (i.e., injury) or internal events (i.e., RNA dyshomeostasis) may trigger nuclear TDP43 egress. In the cytosol, TDP43 undergoes liquid-like condensation, as observed for other RNA-binding proteins in similar environments[91]. At this stage, at least two scenarios are possible. If the stressors are self-limiting and autophagy is functional, mislocalized TDP43 is eliminated through autophagy, and nuclear TDP43 levels are restored through new protein synthesis. Alternatively, if the stressors persist, both existing and newly synthesized pools of TDP43 are mislocalized, accelerating TDP43 accumulation within autophagosomes and lysosomes (**Fig. 7B, C**)[92]. Our data reveal a size-dependent relationship between lysosomes and intraluminal fibrils, with larger fibrils preferentially residing in enlarged lysosomes, suggesting impaired lysosomal processing or lysosomal dysfunction. Fibril nucleation may initiate in smaller lysosomes; subsequent lysosomal fusion and volumetric expansion facilitate continued fibril elongation, leading to the accumulation of larger filamentous aggregates. Although the consequences of TDP43 fibrillization within these organelles remain unknown, several scenarios are possible. As is the case for α-synuclein[93], TDP43 fibrils may escape from lysosomes and seed additional TDP43 aggregation within the cytoplasm. Alternatively, lysosomal TDP43 may be delivered to autophagosomes, where it undergoes either degradative or secretory autophagy; acquired or genetic perturbations may further enhance the latter event, thereby increasing lysosomal/autophagosomal activity[94]. Both possibilities are consistent with disease-associated mutations in autophagy-related genes (i.e., *UBQLN2, C9ORF72, OPTN, SQSTM1*)[95–99], lysosomal trafficking and function (*GRN, CHMP2B*)[100–105], age-related declines in the efficiency of neuronal autophagy, and the broad neuroprotection afforded by autophagy-inducing strategies in ALS/FTLD-TDP models[39,52,53].

Taken together, we establish a cellular model of TDP43 mislocalization and cytoplasmic aggregation, a signature pathologic event in ALS/FTLD-TDP. Using this model, we provide the first visual snapshots *in situ* of TDP43 aggregates within neuronal lysosomes and autophagosomes, highlighting the critical connection between autophagy and the pathogenesis of ALS/FTLD-TDP. We expect this platform to be invaluable not only for investigating the pathogenesis and origins of TDP43 pathology but also for developing strategies to detect and potentially even reverse TDP43 mislocalization in ALS/FTLD-TDP and related TDP43-proteinopathies.

Acknowledgments:

We thank all members of the Barmada, Baldridge, and Mosalaganti laboratories for their advice and suggestions. We thank Dr. Jing Liang and the Microscopy Core of the University of Michigan Biomedical Research Core Facilities for their assistance with the immunogold labeling experiments. We thank Dr. Vinson Lam for his assistance with data collection and segmentation analysis.

Funding:

This work was supported by:

National Institutes of Health DP2GM150019-01 (SM)

National Institutes of Health R01NS097542, R01NS113943 and 1R56NS128110-01 (SJB)

Kissick Family Foundation & Milken Institute Frontotemporal Dementia Grant (SJB & SM)

National Institutes of Health AWD012778 (EP)

National Institutes of Health R35GM128592 (RDB)

National Institutes of Health T32GM007544 (JER)

National Institutes of Health T32GM141840 to (MF)

National Institutes of Health P30AG072931 to the University of Michigan Brain Bank and Alzheimer's Disease Research Center

National Institutes of Health S10OD030275 and the Arnold and Mabel Beckmann Foundation award to the University of Michigan Cryo-EM facility

University of Michigan Pioneer Postdoctoral Fellowship (ALE)

University of Michigan Life Sciences Institute

American Heart Association Predoctoral Fellowship (RS)

Klatskin Sutker Discovery Fund (SM)

The funders had no role in the study design, data collection, analysis, or the content and publication of this manuscript.

Author contributions:

SM and SJB designed the study. ALE designed experiments with SJB and SM. ALE, MLC, MGF, and DA collected data for most experimental studies, analyzed the data, and assembled the figures. MB helped with qPCR analysis and performed the longitudinal survival assays. ALE, MLC, and JER performed the density centrifugation experiments. ESP and DT carried out immunohistochemistry experiments. ALE and MGF carried out cryo-CLEM experiments. RS and ALE performed the segmentation analysis. XS helped with confocal microscopy data analysis. EMHT generated and maintained all the iPSC lines. SJB, RDB, and SM provided resources, funding, and conceptual input for experiments and supervised the research. All authors were involved throughout the research process, agreed amongst themselves regarding roles and responsibilities, and contributed to the review, editing, and approval of the manuscript.

Competing interests:

S.J.B. serves on the advisory board for Neurocures, Inc., Symbiosis, Eikonizo Therapeutics, Ninesquare Therapeutics, the Live Like Lou Foundation, and the Robert Packard Center for ALS Research. S.J.B. has received research funding from Denali Therapeutics, Biogen, Inc., Lysoway Therapeutics, Amylyx Therapeutics, Acelot Therapeutics, Meira GTX, Inc., Prevail Therapeutics, Eikonizo Therapeutics, and Ninesquare Therapeutics.

Data and materials availability:

All correspondence regarding the materials and data presented in this paper should be addressed to sbarmada@med.umich.edu or mosalaga@umich.edu.

Figures (Main, 1-7)

Figure 1. Short GU-rich oligonucleotides induce TDP43 nuclear export, cryptic exon splicing, and neurotoxicity in human iNeurons.
Figure 2. *In situ* cryo-CLEM workflow for ultrastructural analysis of human iNeurons.
Figure 3. Mislocalized TDP43 accumulates within neuronal autophagosomes and lysosomes.
Figure 4. GU-rich oligonucleotides induce TDP43 fibrilization in autophagosomes and lysosomes of HEK293T cells.
Figure 5. TDP43 deposits overlap with lysosomal markers in patient tissue.
Figure 6. Patient brain-derived lysosomal TDP43.
Figure 7. An autophagy-centric model of early-stage TDP43 pathology.

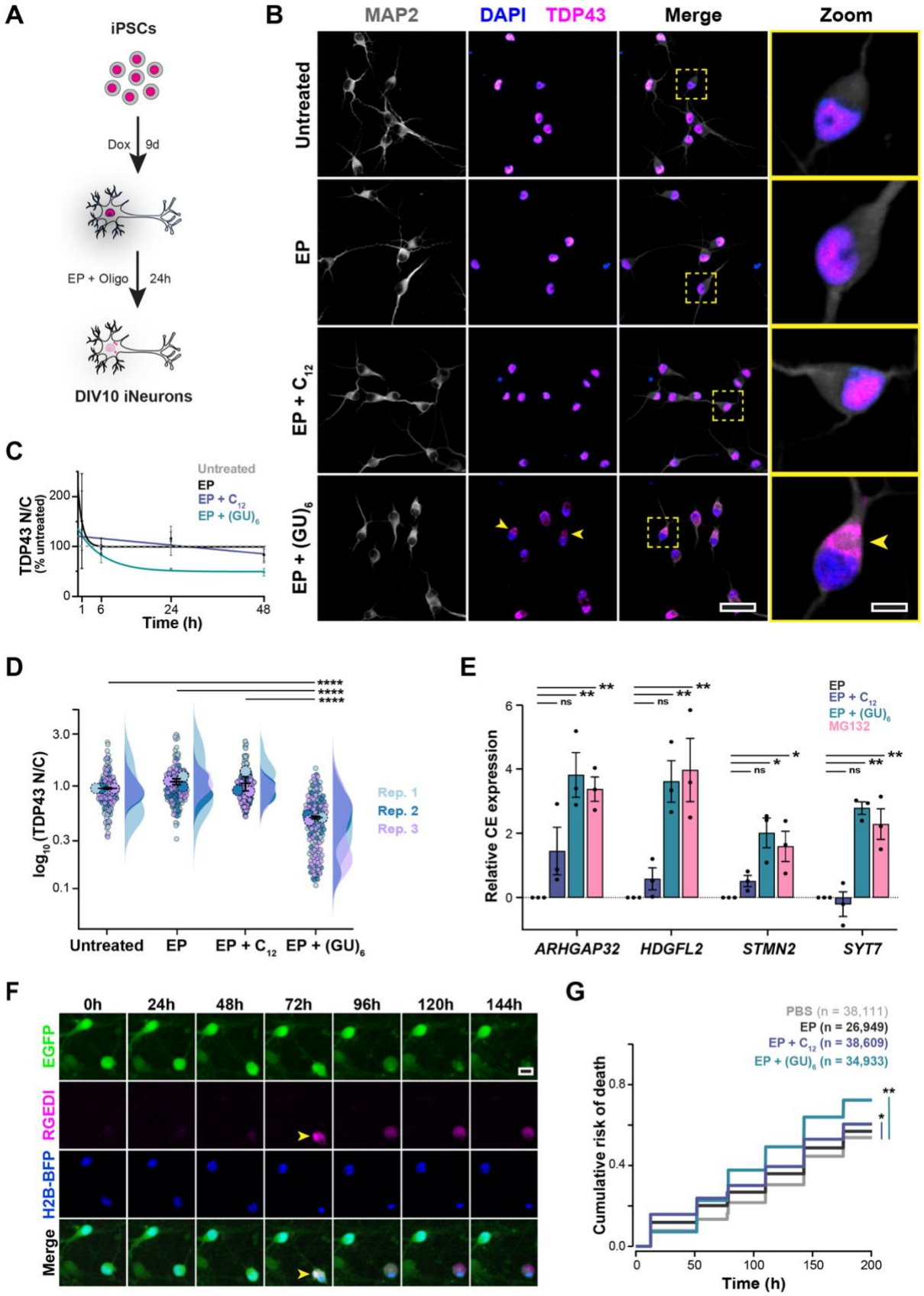
A
iPSCs
Dox
9d
EP + Oligo
24h
DIV10 iNeurons
B
MAP2
DAPI
TDP43
Merge
Zoom
Untreated
EP
EP + C12
EP + (GU)6
C
Untreated
EP
EP + C12
EP + (GU)6
TDP43 N/C (% untreated)
Time (h)
D
log10(TDP43 N/C)
Rep. 1
Rep. 2
Rep. 3
Untreated
EP
EP + C12
EP + (GU)6
E
EP
EP + C12
EP + (GU)6
MG132
Relative CE expression
ARHGAP32
HDGFL2
STMN2
SYT7
F
0h
24h
48h
72h
96h
120h
144h
EGFP
RGEDI
H2B-BFP
Merge
G
PBS (n = 38,111)
EP (n = 26,949)
EP + C12 (n = 38,609)
EP + (GU)6 (n = 34,933)
Cumulative risk of death
Time (h)

Figure 1. Short GU-rich oligonucleotides induce TDP43 nuclear export, cryptic exon splicing, and neurotoxicity in human iNeurons. (A) Schematic outline of RNA-induced TDP43 nuclear egress and cytoplasmic deposition in iPSC-derived neurons. **(B)** Representative confocal fluorescence microscopy images of untreated DIV10 iNeurons (top row) or iNeurons treated with Endo-Porter only (EP, second row), Endo-Porter with control oligo (EP + C_{12}, third row), or Endo-Porter with GU-oligo (EP + $(GU)_6$, last row) for 24h before being chemically fixed and stained for neuronal marker (MAP2), nuclei marker (DAPI), and TDP43. TDP43 mislocalization from the nucleus to cytoplasm was evident only in $(GU)_6$-treated intact iNeurons (last row); yellow arrowheads highlight select iNeurons. A representative iNeuron (yellow dashed box) for each condition is shown at 5× magnification (last column). Images are pseudo-colored as follows: MAP2 (gray), DAPI (blue), and TDP43 (magenta). Scale bar: 50 µm, except for 5× magnified image, which is 10 µm. **(C)** TDP43 nucleus vs. cytoplasm (N/C) fluorescence intensity ratios in DIV10 iNeurons either left untreated (gray dashed line) or treated with EP alone (black), EP with 2µM C_{12} (purple), or EP with 2µM $(GU)_6$ (teal) for 1-48h. N/C ratios for each treatment and time point were normalized to the mean value of the untreated control and reported as percent untreated. (mean ± SEM, n > 48 for all three biological replicates for each treatment and time point, curves were fit to the mean values using non-linear regression with a one-phase exponential decay model). **(D)** Log-transformed ratio of TDP43 fluorescence intensity in the nucleus vs. cytoplasm (N/C ratio) plotted for DIV10 iNeurons either untreated or treated with EP only, EP with 2µM C_{12}, or EP with 2µM $(GU)_6$ for 24h. TDP43 N/C ratios were normalized to the untreated condition for each replicate. (mean ± SEM, Mann-Whitney test, ****$p < 0.0001$, n > 48 for all three biological replicates). Biological replicates 1-3 are colored as light blue, blue, and purple, respectively. **(E)** Quantification of the de novo cryptic exon inclusions, by RT-qPCR analysis for a panel of TDP43 substrates, *ARHGAP32, HDGFL2, STMN2, SYT7* in DIV10 iNeurons treated with either EP (black), EP and 2µM C_{12} (EP + C_{12}, purple), EP and 2µM $(GU)_6$, (EP + $(GU)_6$, teal), or 100nM of potent proteasome inhibitor, MG132 (pink), for 24h. Transcript expression levels were normalized to *GAPDH* transcript levels and the Endo-Porter treated condition for each replicate (mean ± SEM, Tukey test, **$p < 0.01$, *$p < 0.05$, n = 3). **(F)** Human iNeurons were tracked daily for 10d by automated microscopy, visualized using a cell marker (EGFP) in green, nuclear marker (H2B-BFP) in blue, and a red genetically encoded death indicator (RGEDI) in red. Yellow arrowheads at 72h indicate time of death, marked by increases in RGEDI fluorescence, rounding of the cell body, and retraction of neurites. **(G)** Cumulative risk of death in human iNeurons treated with PBS (gray), EP alone, or EP + C_{12} or $(GU)_6$ oligos (2µM each). n = number of neurons, combined from 6 technical replicates per each of the 3 biological replicates. * $p < 2x10^{-16}$, hazard ratio (HR) = 1.09; ** $p < 2x10^{-16}$ HR= 1.22; Cox proportional hazards analysis.

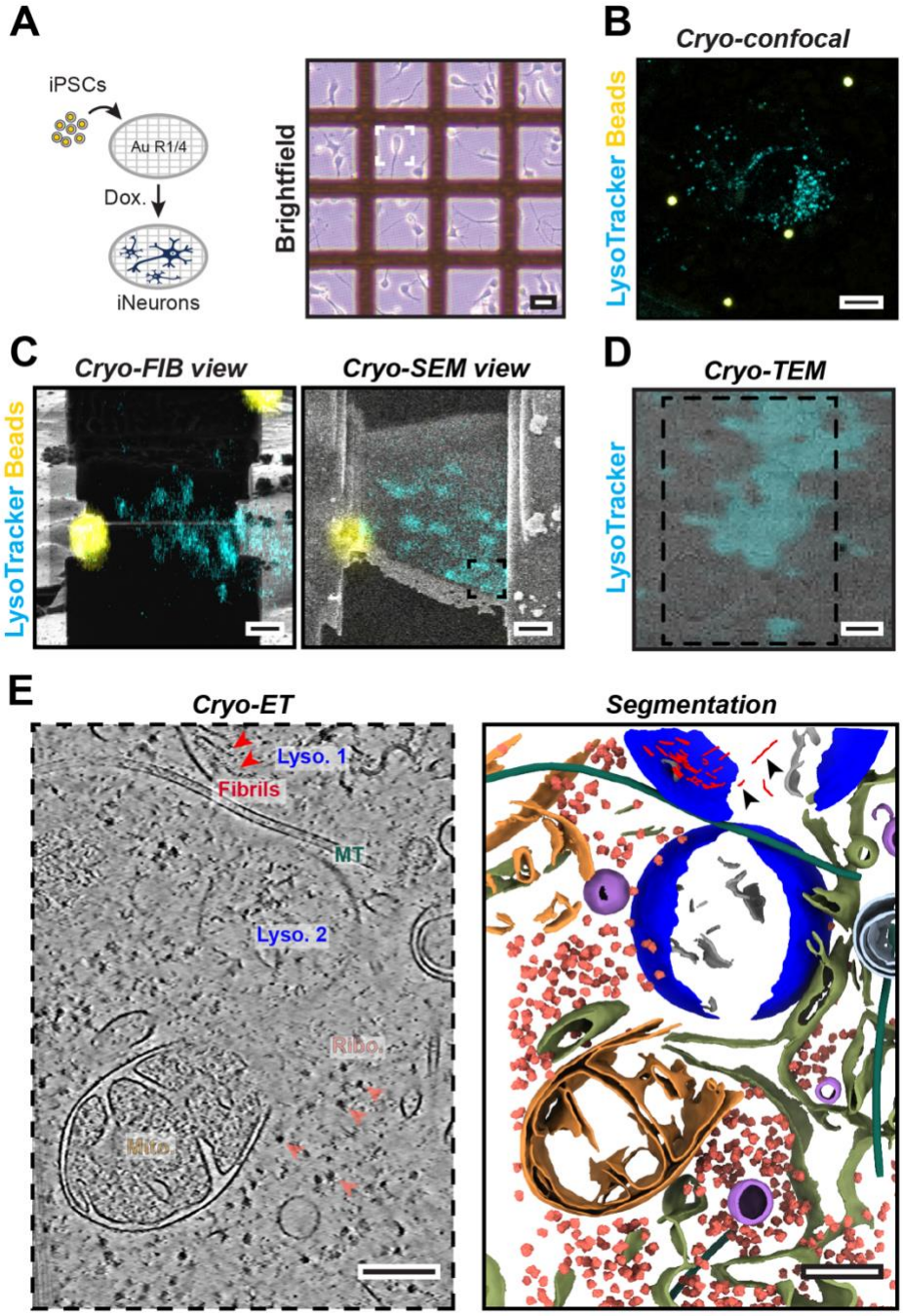

Figure 2. *In situ* cryo-CLEM workflow for ultrastructural analysis of human iNeurons. (**A**) Schematic of doxycycline-inducible iPSCs differentiated to iNeurons on micropatterned electron microscopy grids (left). The grids are manually checked under a widefield microscope for quality and are subsequently plunge-frozen in liquid ethane. Representative widefield image of iNeurons growing on micropatterned grids (right). Scale bar: 50µm. Endo-Porter and $(GU)_6$ oligonucleotides are added to the grids 24 hours before plunge-freezing, LysoTracker is added 5 minutes before, and FluoSpheres (diameter - 2 µm) are added immediately before plunge-freezing. (**B**) A pseudocolored maximum intensity projection image of cryo-confocal z-stack with LysoTracker (cyan), and FluoSphere beads (yellow) collected from an iNeuron (white dashed box in panel A) on a grid for precise correlative cryo-FIB/SEM milling. Scale bar: 10µm. (**C**) Overlay of the cryo-

confocal fluorescence microscopy data onto a lamella milled by correlation through the 3D-correlation toolbox (3DCT). The cryo-FIB view (left) and cryo-SEM view (right) of the same lamella are shown. Scale bar: 2µm. (**D**) Overlay of the z-slice of LysoTracker fluorescence (cyan) and 6500× cryo-TEM montage image of the lamella acquired at the region highlighted in the cryo-SEM view image. Tomography tilt series are collected in the areas of the cryo-lamella highlighted (black dashed rectangle). Scale bar: 200nm. (**E**) Slice through a reconstructed and denoised tomogram showing intact neuronal interiors (left). Neuronal microtubule (MT), lysosome (Lyso. 1 & 2), mitochondria (Mito.), and ribosomes (Ribo.) are readily visible. The fibrils within the top lysosome and the ribosomes are highlighted with red and salmon arrowheads, respectively. Scale bar: 200 nm. The corresponding 3D segmentation (right) highlights cellular features rendered as: ribosomes (salmon), fibrils (red), endoplasmic reticulum (olive green), mitochondria (golden orange), microtubules (dark green), lysosome (blue), degraded cargo (gray), vesicles (lilac), and multivesicular bodies (light blue). Scale bars: 200nm. Fibrillar deposits (black arrowheads) are only observed in one of the two lysosomes in the field of view (Lyso. 1, top).

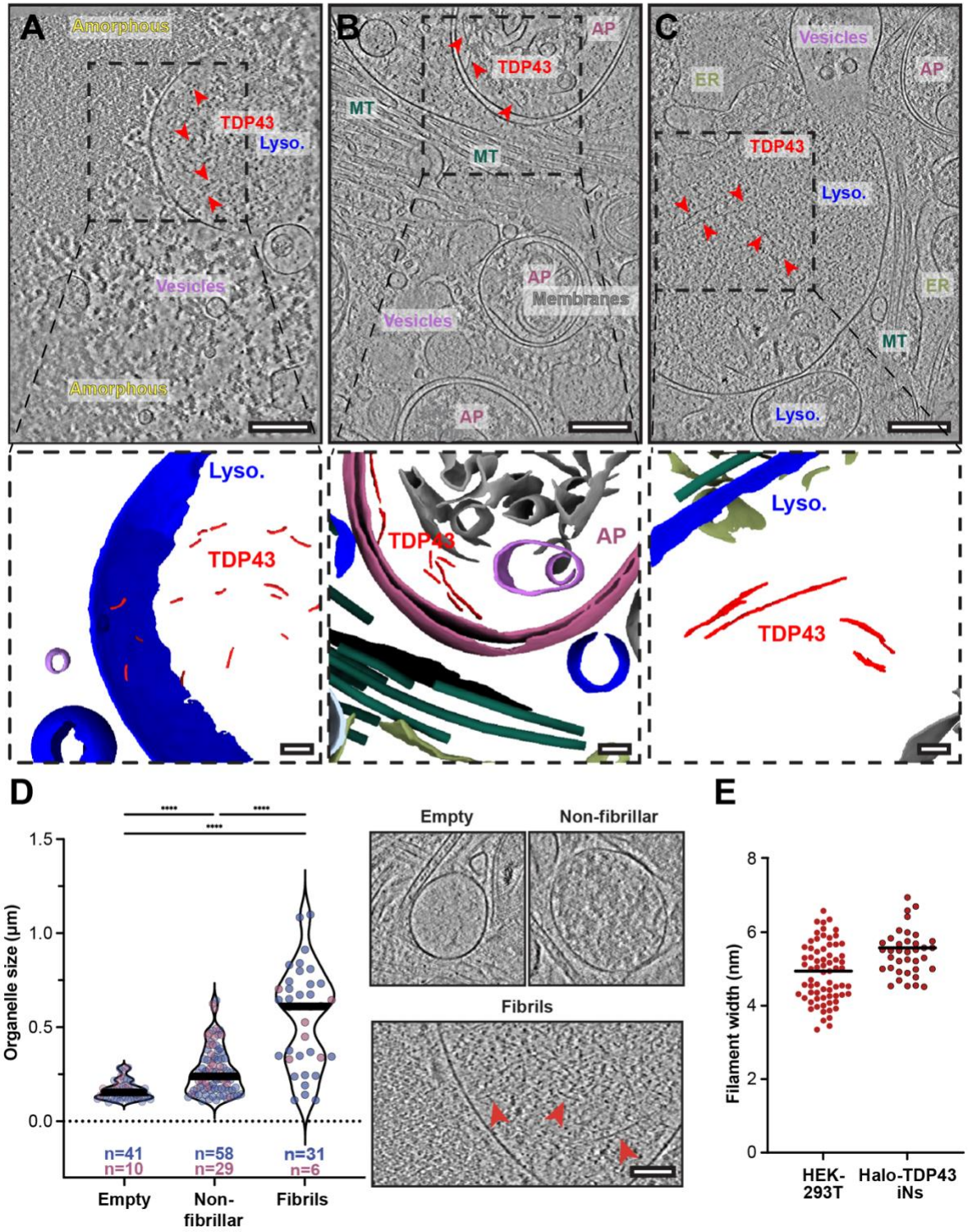

Figure 3. Mislocalized TDP43 accumulates within neuronal autophagosomes and lysosomes. (**A-C**) Top: Slice through reconstructed tomograms from Halo-TDP43 iNeurons treated with EP and $(GU)_6$ oligo showing intact neuronal interiors. Neuronal lysosomes (Lyso.), vesicles, microtubules (MT), autophagosomes (AP), endoplasmic reticulum (ER), 'condensate-like' ribosome-excluded zones (Amorphous), membranes, and TDP43 (red arrowheads) are

highlighted. A representative example of a condensate proximal to a lysosome containing shorter TDP43 fibrils is shown in (**A**), autophagosomes that have engulfed TDP43 fibrils in (**B**), and an enlarged lysosome with TDP43 fibrils is shown in (**C**). Scale bars: 200 nm. Bottom: The corresponding segmentation of the tomograms showing the zoomed-in view of the sub-region highlighted by the dashed black box. Cellular features rendered as: ribosomes (salmon), TDP43 (red), endoplasmic reticulum (olive green), mitochondria (orange), microtubules (dark green), lysosome (blue), membranes (gray), vesicles (lilac), multivesicular bodies or intralumenal vesicles (light blue), plasma membrane (black), and autophagosomes (purple) are highlighted. Scale bars: 100 nm. (**D**) Left: Quantification of organelle size with respect to the luminal content. Single-membraned organelles, either larger than 100nm (indicated by blue circles), and double-membrane bound organelles (indicated by purple circles) were categorized from ~50 tomograms reconstructed from tilt series acquired on lamellae from Halo-TDP43 iNeurons treated with EP and $(GU)_6$ oligo. These organelles were classified based on their internal luminal contents as electron translucent (empty), containing unknown cargo, amorphous or membranous material (non-fibrillar), and bonafide long fibrils (fibrils). Medians are shown as thick lines. Right: Representative slices through tomograms of empty, non-fibrillar or fibril-containing single-membrane-bound organelles. (**E**) Distribution of lysosome-bound filament widths from lysosomes isolated from HEK293T cells (mean ± SD = 4.9 ± 0.79nm, n = 69) and lysosomes within Halo-TDP43 iNeurons (mean ± SD = 5.5 ± 0.61nm, n = 37).

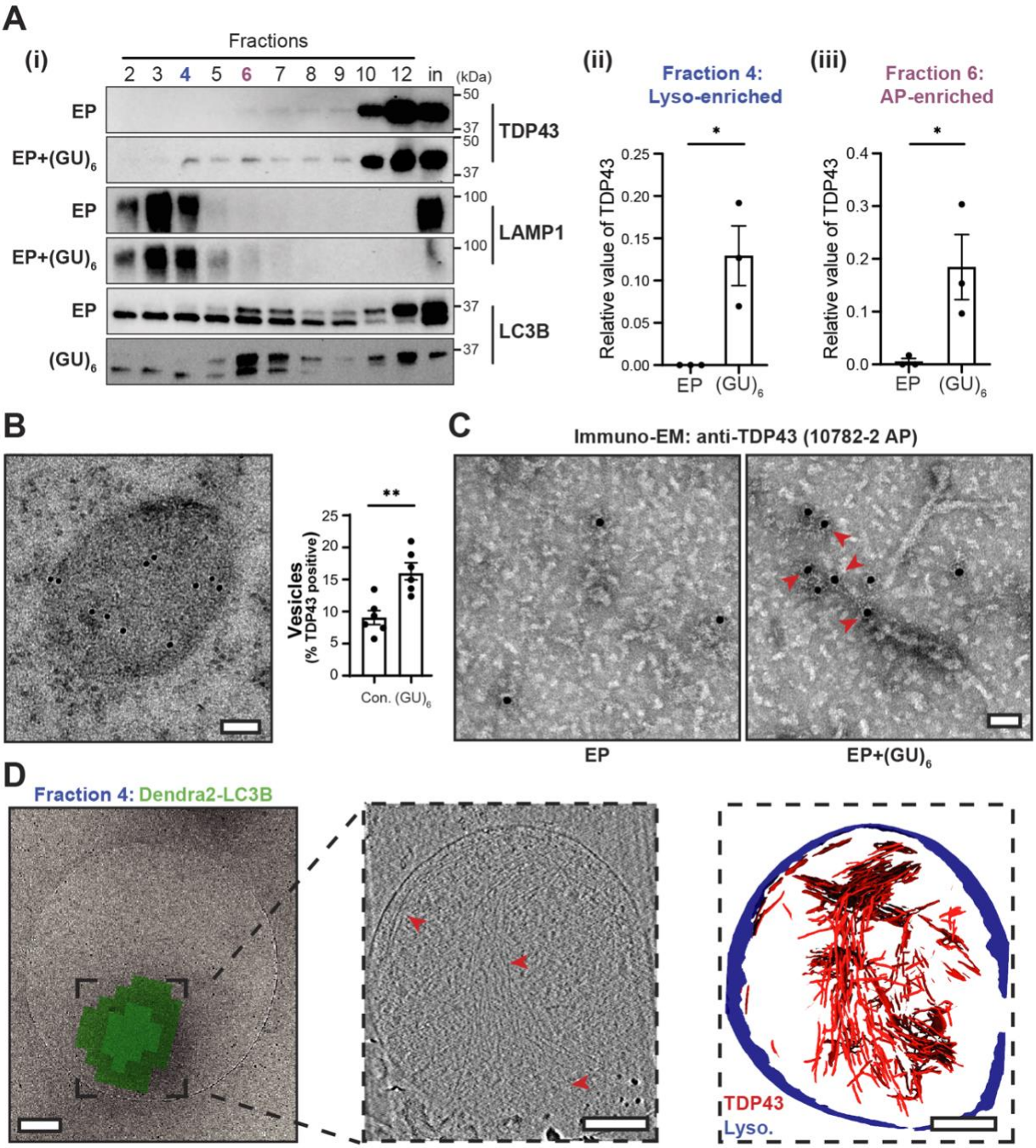

Figure 4. GU-rich oligonucleotides induce TDP43 fibrilization in autophagosomes and lysosomes of HEK293T cells. (**A**) (i) Representative immunoblots of fractions 2-12 and membrane fraction input (in) isolated from Endo-Porter and $(GU)_6$-treated Dendra2-LC3B HEK293T cells, detected with anti-TDP43, -LAMP1, and -LC3B antibodies. n=3. Quantification of TDP43 in fractions 4 (ii) and 6 (iii) (mean ± SEM, ANOVA, Tukey's test, *$p < 0.05$). (**B**) Anti-TDP43 immunogold labeling on an ultrathin section of $(GU)_6$-treated Dendra2-LC3B HEK293T cells (left). n=6. Scale bar, 100nm. Quantification of TDP43-positive vesicles in oligonucleotide-treated Dendra2-LC3B HEK293T cells (right). (Welch's t-test, **$p < 0.01$). (**C**) Representative negative stain EM images of anti-TDP43 immunogold labeled, detergent insoluble TDP43 fibrils isolated from Dendra2-LC3B HEK293T cells. Red arrowheads depict gold beads on fibrils. Scale bar, 50nm. (**D**) Correlative cryo-electron tomography of lysosome-enriched fraction from $(GU)_6$-

treated Dendra2-LC3B HEK293T cells. A representative 6500× cryo-TEM montage image of a lysosome overlaid with the Dendra2-LC3B cryo-fluorescence signal (left). Slice through a reconstructed, denoised tomogram of the same region, highlighting ensconced TDP43 fibrils (red arrowheads, middle). Segmentation of the tomogram with TDP43 fibrils (red) and the lysosome membrane (blue) highlighted (right). Scale bars: 200nm.

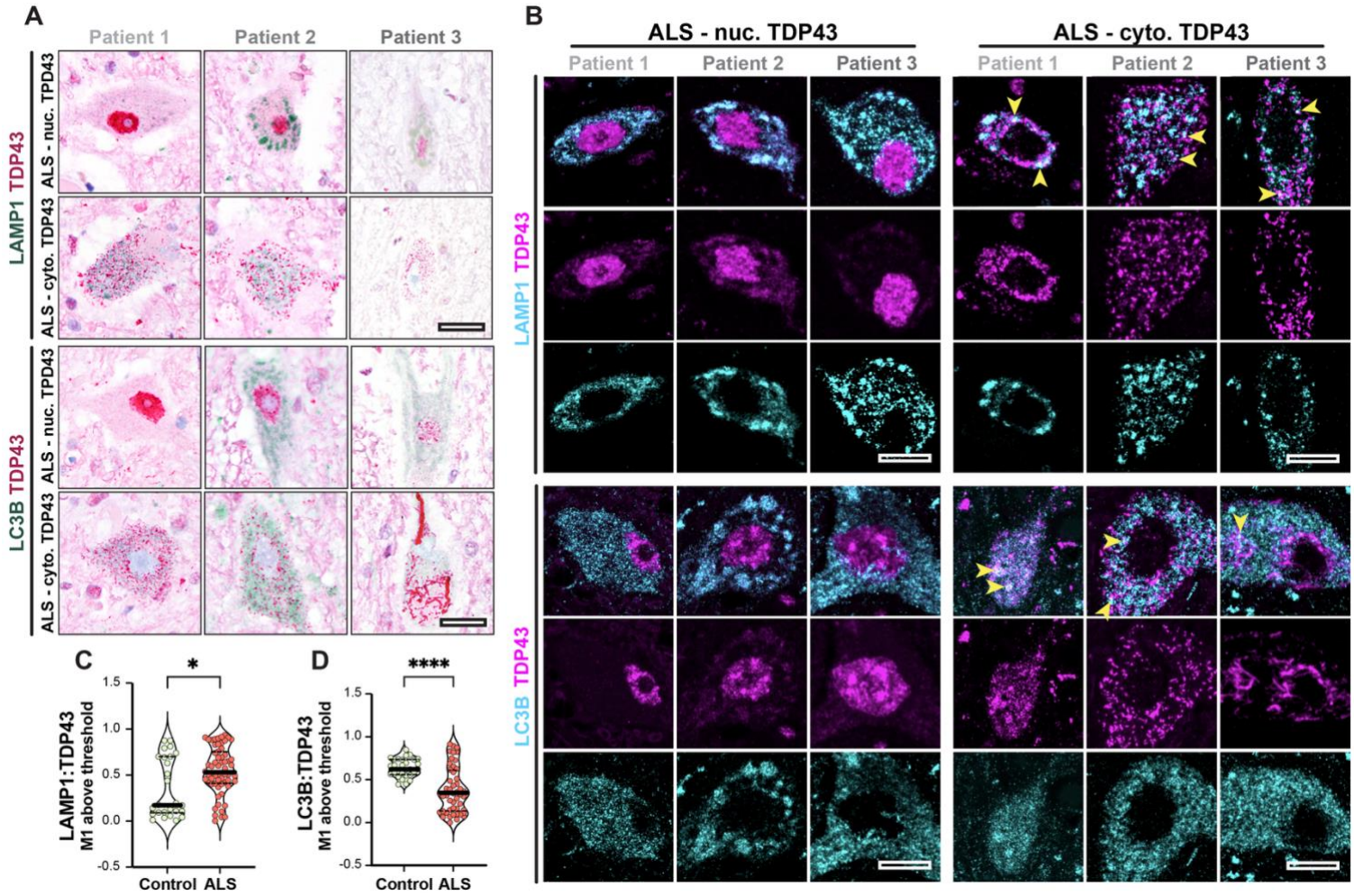

Figure 5. TDP43 deposits overlap with lysosomal markers in patient tissue. (**A**) Immunohistochemical analysis of motor neurons from the spinal cords of three patients (1, 2, 3) with sporadic ALS, showing either TDP43 (magenta) and LAMP1 (green, top) or LC3B (green, bottom). In each case, motor neurons with TDP43 in the nucleus ('ALS–nuc. TDP43', top row) and neurons with mislocalized, cytoplasmic TDP43 ('ALS-cyto. TDP43', bottom row) from the patient are shown. Scale bar, 20 µm. (**B**) Representative images from immunofluorescence analysis of three (patients 1, 2, 3, respectively) post-mortem tissue sections from sporadic ALS patients stained for TDP43 (magenta), LAMP1 (cyan, top half), or LC3B (cyan, bottom half). Motor neurons without TDP43 mislocalization are to the left, and diseased neurons with cytoplasmic TDP43 are to the right. Diseased neurons show colocalization of LAMP1 or LC3B with cytosolic TDP43 (yellow arrowheads, right half, top row). Scale bars, 10 µm. **(C)** Proportion of LAMP1 fluorescence overlapping with TDP43 in control (no disease) and ALS patient tissue sections. Median and quartiles are shown as thick and dashed lines, respectively; Mann-Whitney test, *$p < 0.05$, n=26 and n=60 motor neurons across three control and three ALS patients, respectively. **(D)** Proportion of LC3B fluorescence overlapping with TDP43 in three separate control and ALS patient tissue sections. Median and quartiles are shown as thick and dashed lines, respectively; Mann-Whitney test, ****$p < 0.0001$, n=29 and n=48 motor neurons across three control and three ALS patients, respectively.

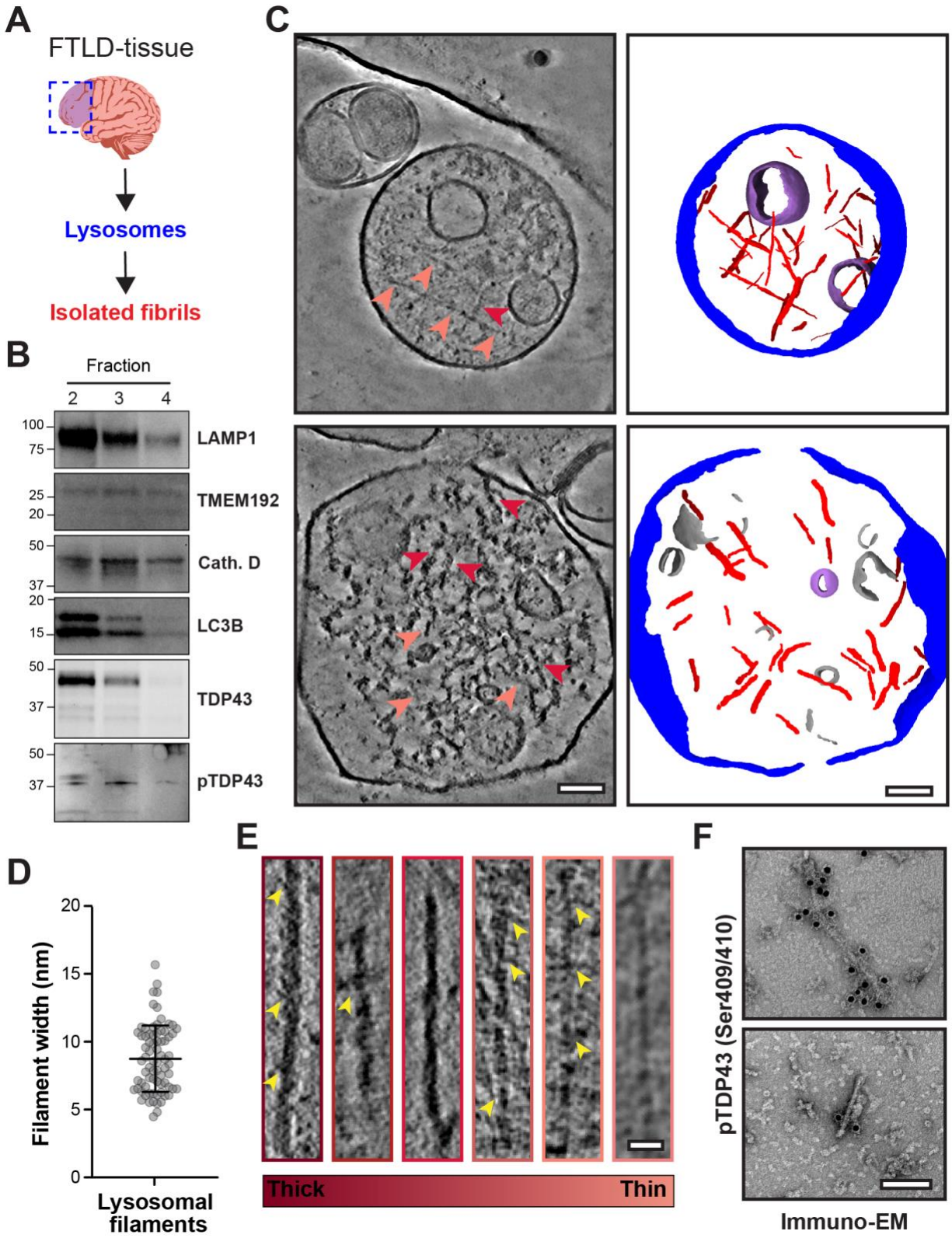

Figure 6. Patient brain-derived lysosomal TDP43. (A) Brief schematic illustration of the workflow for post-mortem brain tissue using serial ultracentrifugation and density gradient fractionation (see Fig. S6 for more details). (**B**) Immunoblots of fractions 2-4 from the density

gradient fractionation of ALS/FTLD-TDP brain-tissue probed for the lysosomal markers LAMP1, TMEM192, and Cathepsin D (Cath. D); autophagosomal marker, LC3B; TDP43 and phospho-TDP43 (pTDP43, S409/410). TDP43 is enriched in autophagosomes and lysosomes, specifically in fraction 2, confirming the presence of multiple proteolyzed TDP43 species. (**C**) Left: slice through two reconstructed and denoised cryo-tomograms of fraction F2, revealing filaments of varying widths and morphology within single-membraned lysosomes. Arrowheads depict filaments of varying widths. Thicker ones are represented in red, while the thinner ones are in light red. Scale bar: 50 nm. Right: Corresponding segmentation and rendering of the tomogram on the left showing lysosomal membrane (blue), TDP43 fibrils (red), unknown membranous cargo (gray), and vesicles (lilac). (**D**) Plot of lysosome-bound filament widths ranging from ~5 to ~15 nm, analyzed from 21 tomograms. (**E**) Gallery of TDP43 filaments within the lysosomes. Slice through the tomograms cropped to show filaments of varying thickness. Yellow arrowheads indicate additional densities branching out of the filaments. Scale bar: 20 nm. (**F**) Immunogold labeling against phosphorylated TDP43 (pTDP43, Ser409/410) on sarkosyl insoluble filaments isolated from the lysosome-enriched fraction (F2). Scale bar: 50 nm.

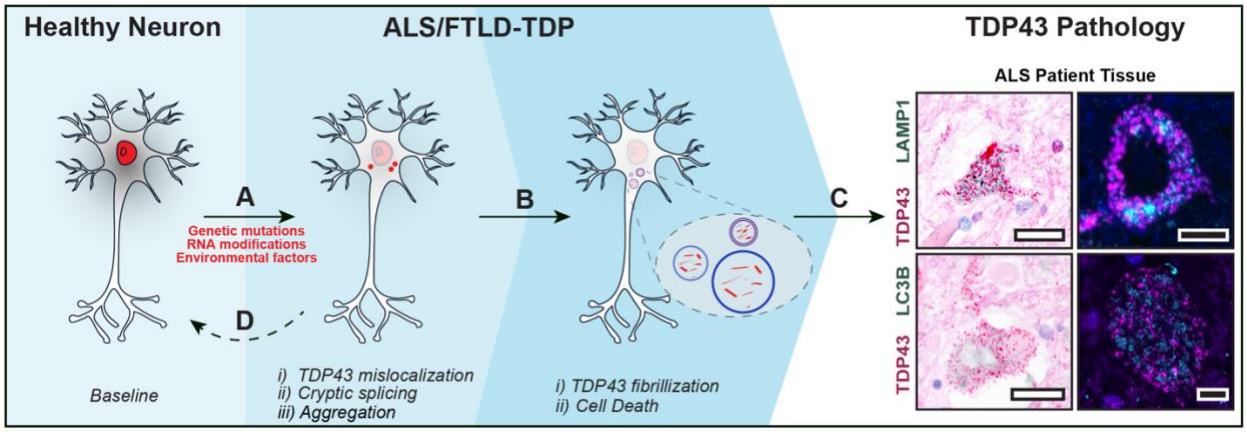

Figure 7. An autophagy-centric model of early-stage TDP43 pathology. (**A**) TDP43 (red) primarily localizes to the nucleus in healthy neurons. RNA misprocessing, genetic mutations, or environmental factors may trigger the nuclear egress and cytosolic accumulation of TDP43. TDP43 nuclear egress disrupts TDP43-dependent splicing activity, and the increased burden of mislocalized TDP43 increases its propensity to aggregate. (**B**) Cellular clearance mechanisms are activated to counteract increasing levels of mislocalized TDP43, resulting in its accumulation in autophagosomes and lysosomes. (**C**) Inevitably, TDP43 mislocalization leads to cytosolic TDP43 fibrilization and neuronal loss, as observed in ALS, FTLD-TDP, and other TDP43 proteinopathies. Representative immunohistochemistry (left) and immunofluorescence (right) images of ALS patient tissue stained for TDP43, LAMP1 (lysosomes, top row), and LC3B (autophagosomes, bottom row). Scale bars: 20μm (left) and 5μm (right). (**D**) Restoring TDP43 nuclear localization, at initial stages, has pharmacotherapeutic potential for preventing TDP43 pathology.

References:

1. Barmada, S. J. Linking RNA Dysfunction and Neurodegeneration in Amyotrophic Lateral Sclerosis. *Neurotherapeutics* **12**, 340–351 (2015).
2. Weskamp, K. & Barmada, S. J. TDP43 and RNA instability in amyotrophic lateral sclerosis. *Brain Research* **1693**, 67–74 (2018).
3. Neumann, M. Molecular Neuropathology of TDP-43 Proteinopathies. *Int J Mol Sci* **10**, 232–246 (2009).
4. Baralle, M., Buratti, E. & Baralle, F. E. The role of TDP-43 in the pathogenesis of ALS and FTLD. *Biochem Soc Trans* **41**, 1536–1540 (2013).
5. Sami J. Barmada & Steven Finkbeiner. Pathogenic TARDBP Mutations in Amyotrophic Lateral Sclerosis and Frontotemporal Dementia: Disease-Associated Pathways. *Reviews in the Neurosciences* **21**, 251–272 (2010).
6. Nelson, P. T. *et al.* Limbic-predominant age-related TDP-43 encephalopathy (LATE): Consensus working group report. *Brain* **142**, 1503–1527 (2019).
7. Neumann, M. *et al.* Ubiquitinated TDP-43 in frontotemporal lobar degeneration and amyotrophic lateral sclerosis. *Science* **314**, 130–133 (2006).
8. Arai, T. *et al.* TDP-43 is a component of ubiquitin-positive tau-negative inclusions in frontotemporal lobar degeneration and amyotrophic lateral sclerosis. *Biochemical and Biophysical Research Communications* **351**, 602–611 (2006).
9. Guenther, E. L. *et al.* Atomic structures of TDP-43 LCD segments and insights into reversible or pathogenic aggregation. *Nature Structural and Molecular Biology* **25**, 463–471 (2018).
10. Cao, Q., Boyer, D. R., Sawaya, M. R., Ge, P. & Eisenberg, D. S. Cryo-EM structures of four polymorphic TDP-43 amyloid cores. *Nature Structural and Molecular Biology* **26**, 619–627 (2019).
11. Berning, B. A. & Walker, A. K. The Pathobiology of TDP-43 C-Terminal Fragments in ALS and FTLD. *Front. Neurosci.* **13**, (2019).
12. Igaz, L. M. *et al.* Enrichment of C-Terminal Fragments in TAR DNA-Binding Protein-43 Cytoplasmic Inclusions in Brain but not in Spinal Cord of Frontotemporal Lobar Degeneration and Amyotrophic Lateral Sclerosis. *The American Journal of Pathology* **173**, 182–194 (2008).
13. Winton, M. J. *et al.* Disturbance of nuclear and cytoplasmic TAR DNA-binding protein (TDP-43) induces disease-like redistribution, sequestration, and aggregate formation. *J Biol Chem* **283**, 13302–13309 (2008).
14. Barmada, S. J. *et al.* Cytoplasmic mislocalization of TDP-43 is toxic to neurons and enhanced by a mutation associated with familial amyotrophic lateral sclerosis. *J Neurosci* **30**, 639–649 (2010).
15. Walker, A. K. *et al.* Functional recovery in new mouse models of ALS/FTLD after clearance of pathological cytoplasmic TDP-43. *Acta Neuropathol* **130**, 643–660 (2015).
16. McDonald, K. K. *et al.* TAR DNA-binding protein 43 (TDP-43) regulates stress granule dynamics via differential regulation of G3BP and TIA-1. *Hum Mol Genet* **20**, 1400–1410 (2011).
17. Liu-Yesucevitz, L. *et al.* Tar DNA binding protein-43 (TDP-43) associates with stress granules: analysis of cultured cells and pathological brain tissue. *PLoS One* **5**, e13250 (2010).
18. Scialò, C. *et al.* Seeded aggregation of TDP-43 induces its loss of function and reveals early pathological signatures. *Neuron* **113**, 1614-1628.e11 (2025).
19. Rummens, J. *et al.* TDP-43 seeding induces cytoplasmic aggregation heterogeneity and nuclear loss of function of TDP-43. *Neuron* **113**, 1597-1613.e8 (2025).
20. Mann, J. R. *et al.* RNA Binding Antagonizes Neurotoxic Phase Transitions of TDP-43. *Neuron* **102**, 321-338.e8 (2019).

21. Duan, L. *et al.* Nuclear RNA binding regulates TDP-43 nuclear localization and passive nuclear export. *Cell Rep* **40**, 111106 (2022).
22. Passos, P. M. dos, Hemamali, E. H., Mamede, L. D., Hayes, L. R. & Ayala, Y. M. RNA-mediated ribonucleoprotein assembly controls TDP-43 nuclear retention. *PLOS Biology* **22**, e3002527 (2024).
23. Zhang, X. *et al.* Multivalent GU-rich oligonucleotides sequester TDP-43 in the nucleus by inducing high molecular weight RNP complexes. *iScience* **27**, 110109 (2024).
24. Tank, E. M. *et al.* Abnormal RNA stability in amyotrophic lateral sclerosis. *Nat Commun* **9**, 2845 (2018).
25. McMillan, M. *et al.* RNA methylation influences TDP43 binding and disease pathogenesis in models of amyotrophic lateral sclerosis and frontotemporal dementia. *Mol Cell* **83**, 219-236.e7 (2023).
26. Li, Y. *et al.* Globally reduced N6-methyladenosine (m6A) in C9ORF72-ALS/FTD dysregulates RNA metabolism and contributes to neurodegeneration. *Nat Neurosci* **26**, 1328–1338 (2023).
27. Arseni, D. *et al.* Structure of pathological TDP-43 filaments from ALS with FTLD. *Nature* **601**, 139–143 (2022).
28. Arseni, D. *et al.* TDP-43 forms amyloid filaments with a distinct fold in type A FTLD-TDP. *Nature* **620**, 898–903 (2023).
29. Finkbeiner, S. The Autophagy Lysosomal Pathway and Neurodegeneration. *Cold Spring Harb Perspect Biol* **12**, a033993 (2020).
30. Nixon, R. A. The aging lysosome: an essential catalyst for late-onset neurodegenerative diseases. *Biochim Biophys Acta Proteins Proteom* **1868**, 140443 (2020).
31. Malik, B. R., Maddison, D. C., Smith, G. A. & Peters, O. M. Autophagic and endo-lysosomal dysfunction in neurodegenerative disease. *Molecular Brain* **12**, 100 (2019).
32. Rubinsztein, D. C., Mariño, G. & Kroemer, G. Autophagy and Aging. *Cell* **146**, 682–695 (2011).
33. Menzies, F. M. *et al.* Autophagy and Neurodegeneration: Pathogenic Mechanisms and Therapeutic Opportunities. *Neuron* **93**, 1015–1034 (2017).
34. Carmona-Gutierrez, D., Hughes, A. L., Madeo, F. & Ruckenstuhl, C. The crucial impact of lysosomes in aging and longevity. *Ageing Research Reviews* **32**, 2–12 (2016).
35. Tan, J. X. & Finkel, T. Lysosomes in senescence and aging. *EMBO reports* **n/a**, e57265 (2023).
36. Rajawat, Y. S., Hilioti, Z. & Bossis, I. Aging: Central role for autophagy and the lysosomal degradative system. *Ageing Research Reviews* **8**, 199–213 (2009).
37. Weskamp, K. *et al.* Shortened TDP43 isoforms upregulated by neuronal hyperactivity drive TDP43 pathology in ALS. *Journal of Clinical Investigation* **130**, 1139–1155 (2020).
38. Chua, J. P. *et al.* Myotubularin-related phosphatase 5 is a critical determinant of autophagy in neurons. *Curr Biol* **32**, 2581-2595.e6 (2022).
39. Safren, N. *et al.* Development of a specific live-cell assay for native autophagic flux. *J Biol Chem* **297**, 101003 (2021).
40. Fernandopulle, M. S. *et al.* Transcription Factor–Mediated Differentiation of Human iPSCs into Neurons. *Current Protocols in Cell Biology* **79**, (2018).
41. Busskamp, V. *et al.* Rapid neurogenesis through transcriptional activation in human stem cells. *Mol Syst Biol* **10**, 760 (2014).
42. Lam, R. S., Töpfer, F. M., Wood, P. G., Busskamp, V. & Bamberg, E. Functional Maturation of Human Stem Cell-Derived Neurons in Long-Term Cultures. *PLOS ONE* **12**, e0169506 (2017).
43. Brown, A.-L. *et al.* TDP-43 loss and ALS-risk SNPs drive mis-splicing and depletion of UNC13A. *Nature* **603**, 131–137 (2022).
44. Ma, X. R. *et al.* TDP-43 represses cryptic exon inclusion in the FTD–ALS gene UNC13A. *Nature* **603**, 124–130 (2022).

45. Zhang, S. *et al.* Acetylation of lysine 82 initiates TDP-43 nuclear loss of function by disrupting its nuclear import. 2024.09.04.611121 Preprint at https://doi.org/10.1101/2024.09.04.611121 (2024).
46. Eersel, J. van *et al.* Cytoplasmic Accumulation and Aggregation of TDP-43 upon Proteasome Inhibition in Cultured Neurons. *PLOS ONE* **6**, e22850 (2011).
47. Weskamp, K., Safren, N., Miguez, R. & Barmada, S. Monitoring Neuronal Survival via Longitudinal Fluorescence Microscopy. *Journal of Visualized Experiments (JoVE)* e59036 (2019) doi:10.3791/59036.
48. Linsley, J. W. *et al.* Genetically encoded cell-death indicators (GEDI) to detect an early irreversible commitment to neurodegeneration. *Nat Commun* **12**, 5284 (2021).
49. Otero, P. C. *et al.* Generation and characterization of monoclonal antibodies against pathologically phosphorylated TDP-43. *PLOS ONE* **19**, e0298080 (2024).
50. Prudencio, M. *et al.* Truncated stathmin-2 is a marker of TDP-43 pathology in frontotemporal dementia. *J Clin Invest* **130**, 6080–6092 (2020).
51. Beckers, J. & Van Damme, P. The role of autophagy in the pathogenesis and treatment of amyotrophic lateral sclerosis (ALS) and frontotemporal dementia (FTD). *Autophagy Reports* **4**, 2474796 (2025).
52. Chua, J. P., De Calbiac, H., Kabashi, E. & Barmada, S. J. Autophagy and ALS: mechanistic insights and therapeutic implications. *Autophagy* **18**, 254–282 (2022).
53. Barmada, S. J. *et al.* Autophagy induction enhances TDP43 turnover and survival in neuronal ALS models. *Nat Chem Biol* **10**, 677–685 (2014).
54. Deng, Z. *et al.* ALS-FTLD-linked mutations of SQSTM1/p62 disrupt selective autophagy and NFE2L2/NRF2 anti-oxidative stress pathway. *Autophagy* **16**, 917–931 (2020).
55. Arnold, J. *et al.* Site-Specific Cryo-focused Ion Beam Sample Preparation Guided by 3D Correlative Microscopy. *Biophysical Journal* **110**, 860–869 (2016).
56. C, B., S, H., J, X., Em, S. & M, L. Heterogeneity of late endosome/lysosomes shown by multiplexed DNA-PAINT imaging. *The Journal of cell biology* **224**, (2025).
57. Grimm, J. B. *et al.* Bright photoactivatable fluorophores for single-molecule imaging. *Nat Methods* **13**, 985–988 (2016).
58. Robinson, S. *et al.* Enhanced legumain activity links progranulin deficiency to TDP-43 pathology in frontotemporal lobar degeneration. 2024.01.16.575687 Preprint at https://doi.org/10.1101/2024.01.16.575687 (2024).
59. Kumar, S. T. *et al.* Seeding the aggregation of TDP-43 requires post-fibrillization proteolytic cleavage. *Nat Neurosci* **26**, 983–996 (2023).
60. Polymenidou, M. *et al.* Long pre-mRNA depletion and RNA missplicing contribute to neuronal vulnerability from loss of TDP-43. *Nat Neurosci* **14**, 459–468 (2011).
61. Tollervey, J. R. *et al.* Characterizing the RNA targets and position-dependent splicing regulation by TDP-43. *Nat Neurosci* **14**, 452–458 (2011).
62. Ling, J. P., Pletnikova, O., Troncoso, J. C. & Wong, P. C. TDP-43 repression of nonconserved cryptic exons is compromised in ALS-FTD. *Science* **349**, 650–655 (2015).
63. Klim, J. R. *et al.* ALS-implicated protein TDP-43 sustains levels of STMN2, a mediator of motor neuron growth and repair. *Nat Neurosci* **22**, 167–179 (2019).
64. Melamed, Z. *et al.* Premature polyadenylation-mediated loss of stathmin-2 is a hallmark of TDP-43-dependent neurodegeneration. *Nat Neurosci* **22**, 180–190 (2019).
65. Seddighi, S. *et al.* Mis-spliced transcripts generate de novo proteins in TDP-43-related ALS/FTD. *Sci Transl Med* **16**, eadg7162 (2024).
66. Kwiatkowski, T. J. *et al.* Mutations in the FUS/TLS gene on chromosome 16 cause familial amyotrophic lateral sclerosis. *Science* **323**, 1205–1208 (2009).
67. Vance, C. *et al.* Mutations in FUS, an RNA processing protein, cause familial amyotrophic lateral sclerosis type 6. *Science* **323**, 1208–1211 (2009).
68. Kim, H. J. *et al.* Mutations in prion-like domains in hnRNPA2B1 and hnRNPA1 cause multisystem proteinopathy and ALS. *Nature* **495**, 467–473 (2013).

69. Johnson, J. O. *et al.* Mutations in the Matrin 3 gene cause familial amyotrophic lateral sclerosis. *Nat Neurosci* **17**, 664–666 (2014).
70. Sreedharan, J. *et al.* TDP-43 Mutations in Familial and Sporadic Amyotrophic Lateral Sclerosis. *Science* **319**, 1668–1672 (2008).
71. Kabashi, E. *et al.* TARDBP mutations in individuals with sporadic and familial amyotrophic lateral sclerosis. *Nat Genet* **40**, 572–574 (2008).
72. Van Deerlin, V. M. *et al.* Common variants at 7p21 are associated with frontotemporal lobar degeneration with TDP-43 inclusions. *Nat Genet* **42**, 234–239 (2010).
73. Coots, R. A. *et al.* m6A Facilitates eIF4F-Independent mRNA Translation. *Mol Cell* **68**, 504-514.e7 (2017).
74. Roundtree, I. A. *et al.* YTHDC1 mediates nuclear export of N6-methyladenosine methylated mRNAs. *eLife* **6**, e31311 (2017).
75. Wang, X. *et al.* N6-methyladenosine-dependent regulation of messenger RNA stability. *Nature* **505**, 117–120 (2014).
76. Sendinc, E. & Shi, Y. RNA m6A methylation across the transcriptome. *Mol Cell* **83**, 428–441 (2023).
77. Deng, J., Chen, X., Chen, A. & Zheng, X. m6A RNA methylation in brain injury and neurodegenerative disease. *Front Neurol* **13**, 995747 (2022).
78. Jiang, L. *et al.* Interaction of tau with HNRNPA2B1 and N6-methyladenosine RNA mediates the progression of tauopathy. *Mol Cell* **81**, 4209-4227.e12 (2021).
79. Yen, Y.-P. *et al.* The motor neuron m6A repertoire governs neuronal homeostasis and FTO inhibition mitigates ALS symptom manifestation. *Nat Commun* **16**, 4063 (2025).
80. Vogler, T. O. *et al.* TDP-43 and RNA form amyloid-like myo-granules in regenerating muscle. *Nature* **563**, 508–513 (2018).
81. Lu, S. *et al.* Heat-shock chaperone HSPB1 regulates cytoplasmic TDP-43 phase separation and liquid-to-gel transition. *Nat Cell Biol* **24**, 1378–1393 (2022).
82. Holehouse, A. S. & Alberti, S. Molecular determinants of condensate composition. *Molecular Cell* **85**, 290–308 (2025).
83. Patni, D. & Jha, S. K. Thermodynamic modulation of folding and aggregation energy landscape by DNA binding of functional domains of TDP-43. *Biochim Biophys Acta Proteins Proteom* **1871**, 140916 (2023).
84. Gu, J. *et al.* Oxidative regulation of TDP-43 self-association by a β-to-α conformational switch. *Proc Natl Acad Sci U S A* **120**, e2311416120 (2023).
85. Al Ojaimi, Y. *et al.* The effect of pH alterations on TDP-43 in a cellular model of amyotrophic lateral sclerosis. *Biochem Biophys Rep* **38**, 101664 (2024).
86. Ormeño, F. *et al.* Chaperone Mediated Autophagy Degrades TDP-43 Protein and Is Affected by TDP-43 Aggregation. *Front Mol Neurosci* **13**, 19 (2020).
87. Yamagishi, T. *et al.* ASO-enhancement of TARDBP exitron splicing mitigates TDP-43 proteinopathies. 2024.07.22.604579 Preprint at https://doi.org/10.1101/2024.07.22.604579 (2024).
88. Lamark, T. & Johansen, T. Aggrephagy: Selective Disposal of Protein Aggregates by Macroautophagy. *International Journal of Cell Biology* **2012**, 736905 (2012).
89. Cho, N. H. *et al.* OpenCell: proteome-scale endogenous tagging enables the cartography of human cellular organization. *Science* **375**, eabi6983 (2022).
90. Guo, W. *et al.* An ALS-associated mutation affecting TDP-43 enhances protein aggregation, fibril formation and neurotoxicity. *Nat Struct Mol Biol* **18**, 822–830 (2011).
91. Maharana, S. *et al.* RNA buffers the phase separation behavior of prion-like RNA binding proteins. *Science* **360**, 918–921 (2018).
92. de Araujo, M. E. G., Liebscher, G., Hess, M. W. & Huber, L. A. Lysosomal size matters. *Traffic* **21**, 60–75 (2020).
93. A, S. *et al.* Neuronal constitutive endolysosomal perforations enable α-synuclein aggregation by internalized PFFs. *The Journal of cell biology* **224**, (2025).

94. Solvik, T. A. *et al.* Secretory autophagy maintains proteostasis upon lysosome inhibition. *J Cell Biol* **221**, e202110151 (2022).
95. Yin, P. *et al.* SQSTM1-mediated clearance of cytoplasmic mutant TARDBP/TDP-43 in the monkey brain. *Autophagy* **18**, 1955–1968 (2022).
96. Renton, A. E., Chiò, A. & Traynor, B. J. State of play in amyotrophic lateral sclerosis genetics. *Nat Neurosci* **17**, 17–23 (2014).
97. Maruyama, H. *et al.* Mutations of optineurin in amyotrophic lateral sclerosis. *Nature* **465**, 223–226 (2010).
98. DeJesus-Hernandez, M. *et al.* Expanded GGGGCC hexanucleotide repeat in noncoding region of C9ORF72 causes chromosome 9p-linked FTD and ALS. *Neuron* **72**, 245–256 (2011).
99. Renton, A. E. *et al.* A Hexanucleotide Repeat Expansion in C9ORF72 Is the Cause of Chromosome 9p21-Linked ALS-FTD. *Neuron* **72**, 257–268 (2011).
100. Clayton, E. L. *et al.* Frontotemporal dementia causative CHMP2B impairs neuronal endolysosomal traffic-rescue by TMEM106B knockdown. *Brain* **141**, 3428–3442 (2018).
101. Wu, J. J. *et al.* ALS/FTD mutations in UBQLN2 impede autophagy by reducing autophagosome acidification through loss of function. *Proc Natl Acad Sci U S A* **117**, 15230–15241 (2020).
102. Beckers, J. *et al.* A toxic gain-of-function mechanism in C9orf72 ALS impairs the autophagy-lysosome pathway in neurons. *Acta Neuropathol Commun* **11**, 151 (2023).
103. Feng, T. *et al.* Loss of TMEM106B and PGRN leads to severe lysosomal abnormalities and neurodegeneration in mice. *EMBO Rep* **21**, e50219 (2020).
104. Tanaka, Y. *et al.* Progranulin regulates lysosomal function and biogenesis through acidification of lysosomes. *Human Molecular Genetics* **26**, 969–988 (2017).
105. Hasan, S. *et al.* Multi-modal proteomic characterization of lysosomal function and proteostasis in progranulin-deficient neurons. *Molecular Neurodegeneration* **18**, 87 (2023).